Accepted for publication in the Astrophysical Journal
Preprint typeset using LaTeX style AASTeX6 v. 1.0

INTERNAL STRUCTURES OF MOLECULAR CLOUDS IN THE LMC REVEALED BY ALMA

Tsuyoshi Sawada[1,2]
Joint ALMA Observatory, Alonso de Córdova 3107, Vitacura, Santiago 763-0355, Chile

Jin Koda
Department of Physics and Astronomy, Stony Brook University, Stony Brook, NY 11794-3800, USA

Tetsuo Hasegawa
National Astronomical Observatory of Japan, National Institutes of Natural Sciences, 2-21-1 Osawa, Mitaka, Tokyo 181-8588, Japan

[1]National Astronomical Observatory of Japan, National Institutes of Natural Sciences
[2]sawada.tsuyoshi@nao.ac.jp

ABSTRACT

We observed five giant molecular clouds (GMCs) in the Large Magellanic Cloud (LMC) in the ^{12}CO $J = 1$–0 line using the Atacama Large Millimeter/submillimeter Array (ALMA). The sample includes four GMCs with some signs of star formation – either YSOs, H II regions, and/or young clusters – and one quiescent GMC without any sign of massive star formation. The data from the ALMA 12 m, 7 m, and Total-Power arrays are jointly deconvolved to obtain high-fidelity images at high spatial resolution ($3'' = 0.7$ pc). The four star-forming GMCs show very complex structures with clumps and filaments. The quiescent GMC shows a relatively diffuse, extended emission distribution without prominent clumps or filaments. This difference is similar to that between structured molecular gas in Milky Way spiral arms and unstructured gas in the inter-arm regions. We characterize the difference with the brightness distribution function and brightness distribution index. In conjunction with other ALMA studies of GMCs in the LMC, the five GMCs tentatively form an evolutionary trend: from less structured, quiescent GMCs to more structured, actively star-forming GMCs. A future ALMA study will be able to map molecular clouds over the LMC and reveal the evolutionary sequence of molecular clouds.

Keywords: galaxies: ISM — galaxies: Magellanic Clouds — ISM: molecules — radio lines: ISM — techniques: image processing

1. INTRODUCTION

Molecular clouds are the site of star formation. Their internal structures and evolution are the key to understanding the process of star formation. Our recent studies of molecular gas in the Milky Way (MW) revealed the structural evolution of the molecular gas when a 1 pc scale is resolved. Sawada et al. (2012a,b) found that the gas in the MW spiral arms is *structured* (i.e., bright and spatially confined, parsec-sized, emission is prominent), while *unstructured* gas (i.e., faint and diffuse) dominates in the inter-arm regions. A similar trend has been found among local star-forming and quiescent molecular clouds (e.g., Kainulainen et al. 2009). In order to characterize these internal structures, Sawada et al. (2012a) introduced two simple tools: the brightness distribution function (BDF) and brightness distribution index (BDI; see Section 6.1).

An extension of such study to external galaxies was, however, limited by the low spatial resolution, typically comparable to the typical size of giant molecular clouds (GMCs), several tens of parsecs, or even worse (e.g., Koda et al. 2009; Schinnerer et al. 2014). Recently, the Atacama Large Millimeter/submillimeter Array (ALMA; Hills et al. 2010) has revolutionized such studies in the Large and Small Magellanic Clouds (LMC and SMC; e.g., Indebetouw et al. 2013). It can resolve the spatial scale relevant to star formation (~ 1 pc; e.g., Lada & Lada 2003) at the distances of the LMC and SMC. Most studies so far have focused on the areas around star-forming regions, e.g., 30 Doradus,

the most active starburst region in the Local Group (Indebetouw et al. 2013; Fukui et al. 2015; Saigo et al. 2017; Nayak et al. 2018), and the H II region N55, which is located within the largest supergiant shell (SGS) in the LMC (Naslim et al. 2018). Molecular clouds in these star-forming environments show complex internal structures, such as clumps and filaments. Muraoka et al. (2017) also showed the presence of small clumps in the star-forming cloud N83C in the SMC. On the contrary, Wong et al. (2017) found a less structured emission distribution in a quiescent molecular cloud in the LMC.

This paper aims to bridge the gap between these two extremes, clouds with very active star formation and those in the quiescent phase, and investigate the evolutionary trend. We observed five clouds in the LMC, which show a range of star formation activity. The properties of the interstellar medium and star formation in the LMC have been thoroughly studied at various wavelengths, thanks to its proximity ($\approx$ 50 kpc; Pietrzyński et al. 2013) and nearly face-on geometry ($i \approx 35°$; van der Marel & Cioni 2001). For this study, it was essential to recover both compact and extended structures. Thus, we combine and jointly deconvolve the data from the ALMA 12 m, 7 m, and Total-Power (TP) arrays.

The presence of CO-dark H_2 is being actively discussed (Greiner et al. 2005; Planck Collaboration 2011). It should be predominantly in the outskirts of GMCs, where the CO is photodissociated by ultraviolet radiation from the outside, while H_2 is optically thick against Lyman-Werner photons and protected. The ALMA observations and discussions in this paper are based on CO observations, and hence are about CO-bright parts of GMCs, not the outskirts.

2. TARGET SELECTIONS

The goal of this paper is to study the evolutionary sequence in cloud structure from relatively quiescent to actively star-forming molecular clouds. Obviously, we can only get a peek at the trend with the limited amount of observing time. Our sample of clouds and field coverages for each cloud are therefore not complete by any means. Nevertheless, we selected five molecular clouds based on the cloud evolutionary stages defined by Kawamura et al. (2009). Their classification is based on the master catalog by Fukui et al. (2008), which consists of 272 clouds in the LMC from the ^{12}CO $J = 1$–0 survey with the NANTEN 4 m telescope at a 2.′6 ($\approx$ 40 pc) resolution. They classified the GMCs into three phases of evolution: Types I (no sign of massive star formation), II (associated with H II regions, i.e., at an early stage of star formation), and III (associated with H II regions and stellar clusters, i.e., at a late stage of star formation). We selected five GMCs at three evolutionary stages; i.e., GMCs 2, 55, and 225 from Type I, GMC 216 from Type II, and GMC 197 from Type III (see Table 1).

Figure 1 illustrates the distribution of our GMCs, as well as the other clouds in the literature. The green circles show the locations of H II regions (Henize 1956) whose surrounding molecular gas was observed with ALMA: 30 Doradus, N159, and N55. These clouds show clumps and filaments (Indebetouw et al. 2013; Fukui et al. 2015; Saigo et al. 2017; Naslim et al. 2018; Nayak et al. 2018). The quiescent cloud, the "Planck cold cloud" (PCC) located near the southern edge of the LMC (green square) was also observed with ALMA (Wong et al. 2017). Our five GMCs, 2, 55, 225, 216, and 197, are distributed from the edge of the disk to near 30 Doradus. We note that GMCs are sometimes referred to by the names of nearby H II regions (e.g., N55, N159), while our GMC IDs (GMC 2, 55, 225, 216, and 197) are from Fukui et al. (2008).

2.1. *Considerations*

Our target selection and observation strategies were built solely on Kawamura et al. (2009) and Fukui et al. (2008). Their results were based on the best information available at the time of their work. Of course, our knowledge has improved, and one may be tempted to modify their GMC classification with respect to star formation. Table 1 lists some other parameters that characterize the star formation activity of our GMCs, in addition to their Kawamura's types based on their association with H II regions and young stellar clusters. For example, the number of young stellar objects (YSOs) within the 30 and 45 pc radii from the center of our ALMA mosaics are zero for GMC 2, but one to four for the other GMCs. With this criterion, GMC 2 (Type I) is the only GMC in our sample that has no sign of star formation, although GMCs 55 and 225 are also classified as Type I. For this, we counted only the YSOs from Seale et al. (2014) with a high likelihood ("probable" ones) of being in the LMC.

The average dust temperature within a field of view (FoV) traces the radiation field. It is also higher ($T_{\rm dust} > 20$ K) for GMCs 55, 197, and 216 than for GMCs 2 and 225 (Gordon et al. 2014). The 8 μm flux is mainly from the interstellar polycyclic aromatic hydrocarbons (PAHs) excited by the background radiation. Hence, it also indicates the strength of the background radiation field. The background 8 μm flux in the table is calculated from the *Spitzer Space Telescope* 8 μm images (Meixner et al. 2006) after removing point sources (i.e., stars). Again, it is higher for GMCs 55, 197, and 216 than for GMCs 2 and 225 (Figure 2).

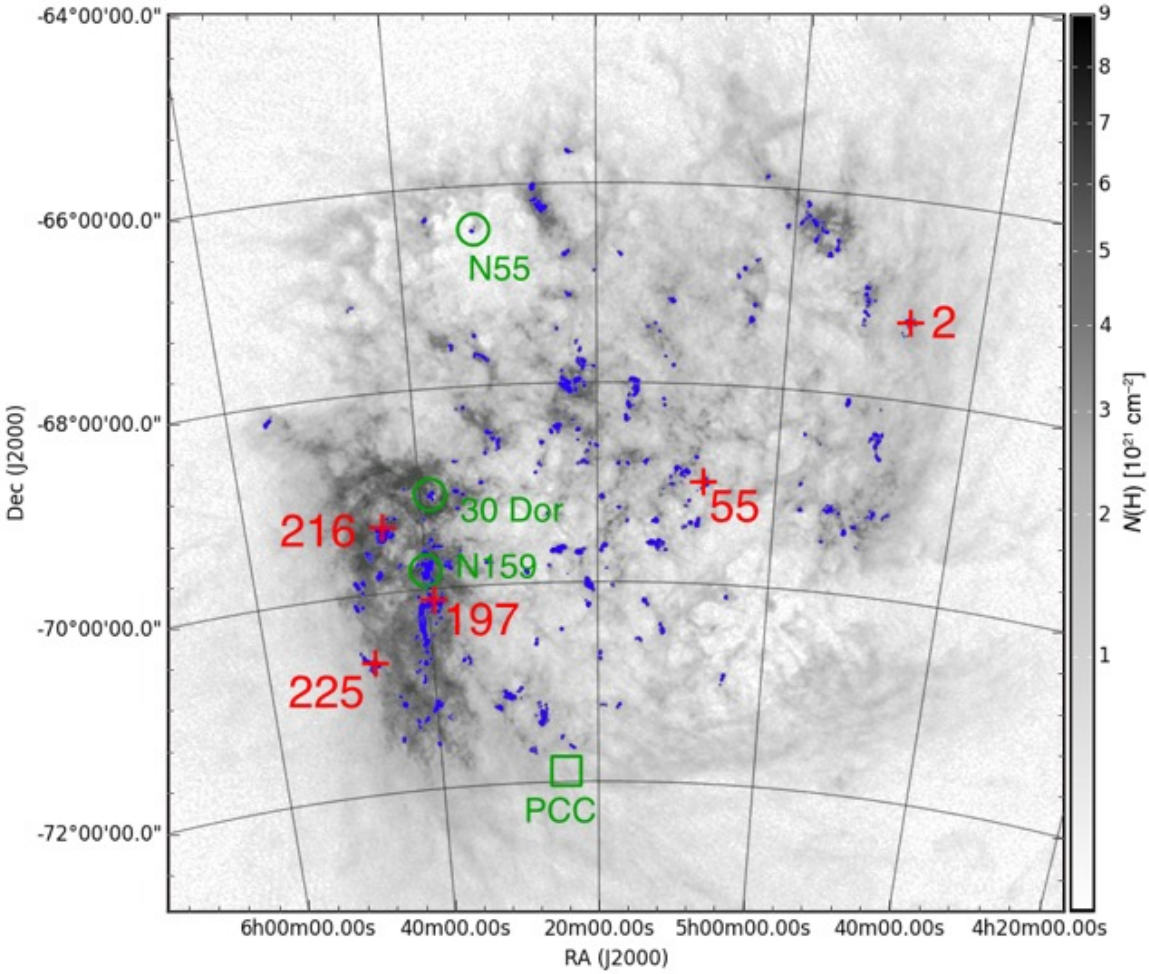

Figure 1. The positions of the target GMCs are shown as red crosses overlaid on the H I (grayscale; Kim et al. 2003; Staveley-Smith et al. 2003) and CO (blue; Wong et al. 2011) distributions. Green circles and squares are the locations of the GMCs with ALMA observations published so far (see the text).

Depending on the adopted indicator of star formation activity, the classification of the GMCs may be altered. This study has this type of uncertainty. From the above parameters, GMC 2 is the only target that does not show any sign of star formation. The other four GMCs show some sign, though some may be at an earlier stage of star formation than the others.

In addition, our ALMA FoVs were set around the peak positions in the CO $J = 1$–0 maps at the 2.′6 resolution (Kawamura et al. 2009). The follow-up CO $J = 1$–0 observations at a higher resolution (45″; Wong et al. 2011) resolved structures further. It turned out that in some cases, the emission peaks at the 2.′6 resolution are not the peaks at the 45″ resolution (Figure 2). Therefore, our ALMA FoVs are not optimal in terms of the peak positions in the 45″ resolution maps. Despite these retrospective considerations, the new ALMA data presented here show a tentative trend of cloud evolution.

Table 1. Parameters of the Sample GMCs

GMC ID[a]	R[a] (pc)	$M_{\rm CO}$(all)[a] ($10^5 M_\odot$)	Type[b]	$N_{\rm YSO,30/45}$[c]	$T_{\rm dust}$[d] (K)	$S_{8\ \mu{\rm m}}$[e] (Jy)	$f_{\rm mol}$[f]	SGS Assoc.[g]
2	97	10	I	0/0	16.5	0.59	0.79	No
55	39	5	I	1/3	20.4	1.07	0.83	Rim

Table 1 continued on next page

Table 1 *(continued)*

GMC ID[a]	R[a] (pc)	$M_{\rm CO}$(all)[a] ($10^5 M_\odot$)	Type[b]	$N_{\rm YSO,30/45}$[c]	$T_{\rm dust}$[d] (K)	$S_{8\ \mu{\rm m}}$[e] (Jy)	$f_{\rm mol}$[f]	SGS Assoc.[g]
197	220	100	III	1/2	22.4	1.80	0.86	Rim
216	80	20	II	2/4	24.4	1.51	0.89	Inside
225	73	10	I	1/1	17.8	0.74	0.70	No

[a] From the NANTEN survey (Fukui et al. 2008)

[b] Type I – no sign of massive star formation; Type II – associated with H II regions; and Type III – associated with H II regions and stellar clusters; Kawamura et al. (2009)

[c] The number of "probable" YSOs (Seale et al. 2014) within 30 and 45 pc radii from the center of our FoVs.

[d] Gordon et al. (2014)

[e] Meixner et al. (2006)

[f] The molecular gas fraction (H I from Kim et al. 2003; Staveley-Smith et al. 2003, ; CO from this work). A CO-to-H_2 conversion factor of 7×10^{20} cm^{-2} (K km s^{-1})$^{-1}$ is assumed (Fukui et al. 2008)

[g] The SGS identification by Dawson et al. (2013) is adopted

3. OBSERVATIONS

The target five GMCs were observed with ALMA using the Band 3 receivers (Claude et al. 2008) as the Early Science Cycle 1 project 2012.1.00641.S. The observations using the 12 m array, which consisted of twenty-seven 12 m antennas and the 64-input correlator (Escoffier et al. 2007), were made in 2013 December. A 469 MHz wide, 3840-channel, dual-polarization spectral window (244 kHz = 0.64 km s^{-1} resolution) was placed at the frequency of the CO $J = 1$–0 line (rest frequency 115.271 GHz) in one of the four basebands. Three 2 GHz wide low spectral resolution spectral windows were set up in the remaining basebands as a serendipitous search for continuum emission, but resulted in no detections. The FoV of $\approx 2\farcm5 \times 2\farcm5$ for each GMC was covered by a 27-pointing mosaic. The total on-source integration time per object was typically 540 s (20 s per mosaic pointing), and the u–v distance typically ranged from 14 to 450 m. The gain calibration was made by observing the QSO J0635−7516 at a typical interval of 8 minutes. Either Uranus or the radio galaxy J0519−4546, whose flux was monitored by the observatory, was observed in each execution as the flux calibrator. The typical system noise temperature $T_{\rm sys}$ at the frequency of the CO line was 170 K.

The shorter u–v distance range was fulfilled by observations using the 7 m array, a part of the Atacama Compact Array (ACA; Iguchi et al. 2009). These observations were done in 2013 November–December and 2014 April using eight to eleven 7 m antennas and the ACA correlator (Kamazaki et al. 2012). The spectral setup was equivalent to that for the 12 m array. The number of mosaic pointings was 10 for each GMC. The typical total on-source integration time and u–v distance were 1000 s (100 s per mosaic pointing) and 7–35 m, respectively. A gain calibrator, QSO J0635−7516 in most cases, was observed at a typical interval of 10 minutes. Either a solar system object (Mars, Uranus, Callisto, Ganymede, or Pallas) or J0519−4546 was used as the flux calibrator. The typical $T_{\rm sys}$ was 120 K.

The even shorter u–v spacing was complemented by filled-aperture (single-dish) observations with the TP array, which was also a part of the ACA. The TP array observations were carried out in 2015 May and June using two or three 12 m antennas and the ACA correlator. A $225'' \times 225''$ FoV for each GMC was mapped using the on-the-fly observing technique. A line-free reference position was visited before every raster row. The QSO 3C 279 was also observed to determine the antenna gains (Jy K^{-1}). The typical total on-source time (per antenna) and $T_{\rm sys}$ were 60 minutes and 140 K, respectively.

4. DATA REDUCTION

Interferometer visibilities and single-dish maps from the ALMA 12 m, 7 m, and TP arrays were delivered by the observatory and were calibrated using the Common Astronomy Software Applications (CASA; McMullin et al. 2007). We subtracted spectral baselines from the delivered TP map by fitting straight lines to emission-free channels. We also applied the correction for the weights of 12 and 7 m visibilities with the `statwt` task in CASA as described in the

CASA guide[1].

A better-filled u–v coverage is always advantageous in deconvolution. We combined the 12 m, 7 m, and TP data in u–v space and deconvolved them jointly. We converted the TP map into visibilities by using the Total Power to Visibilities (TP2VIS) package that runs on the CASA platform[2]. This procedure is discussed and tested in depth in our previous paper (Koda et al. 2011). Here, we briefly describe the essence of this procedure. TP2VIS generates a Gaussian visibility distribution, so that when it is Fourier transformed its dirty image and beam represent the TP map and primary beam, respectively. The optimal weight of the TP visibilities with respect to 12 and 7 m ones can be debated. We adopted the TP weight that corresponds to the rms noise in the TP map. This way the weights represent the quality of data properly.

For deconvolution, we used the Multichannel Image Reconstruction, Image Analysis, and Display (Miriad) software package (Sault et al. 1995), instead of CASA. The `clean` and `tclean` tasks in CASA (as of version 5.3) use only one dirty beam for a whole mosaic in their minor cycles, while it varies across the mosaic. This often causes a divergence in flux and/or artificial stripping patterns[3]. Therefore, we could not use CASA for imaging. All of the visibilities were converted to the MIRIAD data format and were inverted to dirty map and beam with the natural weighting. We ran the `mossdi2` task for image-based clean. We set the number of iterations to 4 million and the `gain` parameter to 0.05.

It is often a problem that the flux of the cleaned map is not consistent with that of the TP map. This is because the two components in the cleaned map use two different beams – the model component uses a convolution beam, while the residual component uses the dirty beam. The areas of the two beams are often not the same, which leads to errors in brightness and flux. To circumvent this problem, we used the residual scaling scheme of Jorsater & van Moorsel (1995).

The convolution beams for the five GMCs are typically an ellipse with a major axis size of 2.″2–2.″6. For analyses on an equal basis, we smoothed the maps to a common 3.″0 resolution (0.73 pc) along both the major and minor axes of the beams. We use a velocity channel spacing of 1 km s^{-1}, at which the sensitivity ranges between 0.47 and 0.67 K (45–66 mJy beam^{-1}).

5. RESULTS

The CO $J = 1$–0 integrated and peak intensity maps are shown in Figure 2. Each CO $J = 1$–0 map covers a $2.'6 \times 2.'8$ (38×41 pc^2) region. A scale bar is in one of the bottom panels. We also show a pseudo-color image from *Spitzer* (24, 8.0, 3.6μm in R, G, B, respectively) and contours from the Mopra CO $J = 1$–0 integrated intensity (Wong et al. 2011). YSO candidates are also marked. The thick white lines indicate the areas of the ALMA CO $J = 1$–0 observations. The centers of our ALMA mosaics were set at the peak positions in Kawamura et al. (2009), which later turned out to not coincide with the peaks at the higher-resolution Mopra CO $J = 1$–0 map. The velocity channel maps are presented in Figures 3–7.

The parameters of the GMCs derived in this paper are listed in Table 2. We adopt a CO-to-H_2 conversion factor of 7×10^{20} cm^{-2} (K km s^{-1})$^{-1}$ (Fukui et al. 2008). The masses within the ALMA fields range between 1.1 and $4.9 \times 10^5 M_\odot$; 5–30% of the total GMC masses in the NANTEN catalog. Below, we note characteristics of individual GMCs.

GMC 2: : This cloud is classified as Type I, without sign of massive star formation, by Kawamura et al. (2009). Indeed, it does not have YSOs (Seale et al. 2014). From the channel maps, the total line width (full-width zero intensity; FWZI) is ≈ 15 km s^{-1}. We find no bright emission (> 10 K). At the lower velocity (248–254 km s^{-1}) fluffy emission is distributed over the FoV. The typical brightness temperature is 3–5 K. At 255–259 km s^{-1} a $\approx$ 15 pc blob dominates. It is rather featureless, i.e., its brightness temperature is more or less uniform (3–5 K).

GMC 55: : Type I, but having YSOs, and hence star forming. The total line width (FWZI) is ≈ 25 km s^{-1}. Possibly, there are two velocity components. The most prominent structure in the lower velocity range (245–257 km s^{-1}) is a filament, or a chain of compact clumps separated by ≈ 5 pc, stretching from the NE to W of the FoV. The width of the filament, or the typical size of the clumps, is ≈ 2 pc, and the length (in the FoV) is ≈ 30 pc. There is a velocity gradient along the filament (several km s^{-1} over 30 pc). The line width is a few km s^{-1} at each portion along the filament. There might be another filament, or a chain of clumps, near the SW corner running from the middle of the western edge toward the SE. At a higher velocity (255–269 km s^{-1}) there is an elongated

[1] https://casaguides.nrao.edu/index.php/DataWeightsAndCombination

[2] https://github.com/tp2vis/distribute/blob/master/README.md

[3] https://casaguides.nrao.edu/index.php/M100_Band3_Combine_4.3

($\approx 10 \times 2$ pc) bright (≈ 14 K) clump with a sharp boundary in the SE of the FoV. Its line width (FWZI) is $\approx 15\,\mathrm{km\,s^{-1}}$.

GMC 197: : Type III with both H II regions and young star clusters. The total line width (FWZI) is $\approx 25\,\mathrm{km\,s^{-1}}$. There may be two velocity components. Emission at the bottom of the FoV shows up at $218\,\mathrm{km\,s^{-1}}$ and this structure persists until $232\,\mathrm{km\,s^{-1}}$ or so ($15\,\mathrm{km\,s^{-1}}$ width). At $224\,\mathrm{km\,s^{-1}}$, filamentary structures start to appear, generally elongated in the N–S direction. There is a bright spot in one of them (R.A. $\approx 5^{\mathrm{h}}39^{\mathrm{m}}52^{\mathrm{s}}$, decl. $\approx -70^\circ06'45''$) that has $\approx 15\,\mathrm{km\,s^{-1}}$ line width and a NW-to-SE velocity gradient. It looks like filaments are spreading radially from around that spot at 228–229 $\mathrm{km\,s^{-1}}$. The filaments merge into a ≈ 20 pc blob seen at 224–234 $\mathrm{km\,s^{-1}}$. After that blob is gone, another blob appear in the south, with a several $\mathrm{km\,s^{-1}}$ line width.

GMC 216: : Type II with H II regions and YSOs. The total line width (FWZI) is $\approx 15\,\mathrm{km\,s^{-1}}$. At lower velocities (221–225 $\mathrm{km\,s^{-1}}$), at least four filamentary structures are apparent and form a web. Along the eastern boundary of the map, there is one filament stretching straight from N to S (R.A. $\approx 5^{\mathrm{h}}44^{\mathrm{m}}47^{\mathrm{s}}$). Two filamentary structures run from NEE to W and SE to W, and apparently merge near the western boundary to form a ≈ 15 pc blob with a line width of several $\mathrm{km\,s^{-1}}$. These structures evolve into more spatially extended blobs at higher velocities (226–230 $\mathrm{km\,s^{-1}}$). Hence, it is not clear if they are filaments, or parts of blobs with large velocity widths. They may be shearing surfaces of, e.g., cloud–cloud collisions. There is another shorter, 10 pc scale, filament that runs in parallel to and north of the NEE–W filamentary structure. At 225–231 $\mathrm{km\,s^{-1}}$ the emission mostly fills the FoV (typically 5–10 K, with some bright spots).

GMC 225: : Type I, but having YSOs and star formation. The total line width (FWZI) is $\approx 10\,\mathrm{km\,s^{-1}}$. There are two components, one in the N and the other in the S. One is a ≈ 15 pc blob in the NW (which may extend beyond the FoV). The velocity range is 213–223 $\mathrm{km\,s^{-1}}$. The brightness is moderately high (≈ 10 K) in its northern half and lower (≈ 5 K) in the south. The southern component is at 216–221 $\mathrm{km\,s^{-1}}$. It may consist of two filaments running parallel to each other. They have a roughly 15×2 pc geometry within the FoV.

Table 2. The Observed Quantities for the Sample GMCs

GMC ID	Center of FoV		RMS[a]	M_{CO}(ALMA)[b]	f_{CO}[c]	BDI
	R.A.(J2000)	Decl.(J2000)	(K)	($10^5 M_\odot$)		
2	$4^{\mathrm{h}}47^{\mathrm{m}}35^{\mathrm{s}}$	$-67^\circ13'00''$	0.46	1.3	0.1	$-\infty$
55	$5^{\mathrm{h}}07^{\mathrm{m}}45^{\mathrm{s}}$	$-68^\circ59'30''$	0.54	1.4	0.3	−0.92
197	$5^{\mathrm{h}}39^{\mathrm{m}}50^{\mathrm{s}}$	$-70^\circ07'00''$	0.57	4.7	0.05	−1.50
216	$5^{\mathrm{h}}44^{\mathrm{m}}35^{\mathrm{s}}$	$-69^\circ26'00''$	0.47	4.9	0.2	−0.83
225	$5^{\mathrm{h}}47^{\mathrm{m}}20^{\mathrm{s}}$	$-70^\circ41'30''$	0.67	1.1	0.1	−1.55

[a] At $3'' \times 3'' \times 1\,\mathrm{km\,s^{-1}}$ resolution

[b] A CO-to-H_2 conversion factor of $7 \times 10^{20}\,\mathrm{cm^{-2}\,(K\,km\,s^{-1})^{-1}}$ is assumed (Fukui et al. 2008)

[c] The fraction of the CO luminosity in the ALMA FoV over that of the entire GMC (Fukui et al. 2008)

6. DISCUSSION

We observed five GMCs in the LMC along the GMC evolutionary stages classified by Kawamura et al. (2009). As discussed in Section 2, additional information became available after this work started, showing YSOs in GMC 55 and 225, which were originally classified as Type I (no sign of massive star formation). Among the five, only GMC 2 does not show any sign of star formation. In addition, it turned out that our FoVs do not optimally cover the target GMCs. Even though our ALMA mosaics are large ($2\farcm6 \times 2\farcm8$; or 38×41 pc^2), the emission peaks at the $45''$ resolution (Wong et al. 2011) were considerably offset from the peaks at the $2\farcm6$ resolution (Fukui et al. 2008). With these limitations in mind, there still seems to be a trend of GMC evolution, when our observations are viewed in the context of work in the literature.

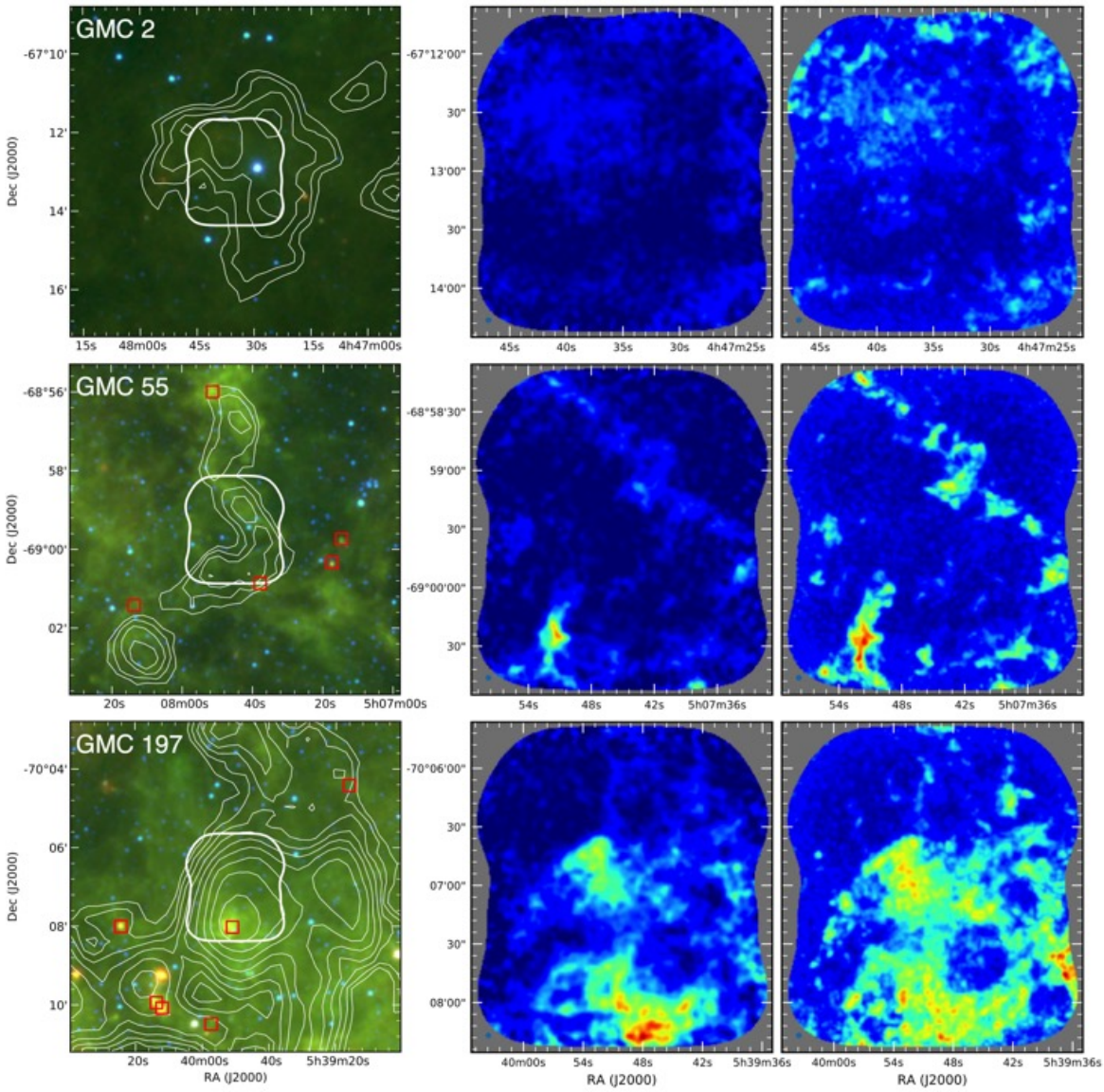

Figure 2. Left: Contours of Mopra CO $J = 1$–0 integrated intensity (2, $2\sqrt{2}$, 4, ..., $32\sqrt{2}$ K km s^{-1}; Wong et al. 2011) toward GMCs 2, 55, 197, 216, and 225 (each row), overlaid on *Spitzer* 24–8.0–3.6 μm three-color images (Meixner et al. 2006). Thick white lines show the ALMA FoVs. The red squares indicate the locations of "probable" YSOs (Seale et al. 2014). Middle: The ALMA CO $J = 1$–0 integrated intensity maps. Right: The ALMA CO $J = 1$–0 peak intensity maps. The ALMA FoVs are $\approx 2\farcm6 \times 2\farcm8$ (or 38×41 pc^2). The spatial resolution ($3''$) is indicated by the blue dots at the bottom left corner of each panel.

6.1. *The Brightness Distribution Function and Index*

The maps of the five GMCs (Figure 2) clearly show less developed internal structures in GMC 2 than in the others. GMC 2 is the one without any sign of star formation, while the others have some associated YSOs.

In order to characterize the visual difference in internal structures, Sawada et al. (2012a) introduced simple tools: the BDF and BDI. The BDF is a histogram of the brightness of a line emission, which quantitatively represents the map appearance. It is defined in α–δ–v space as the fraction of the "pixels" with brightness between T and $T + dT$. The BDI is a single number that represents the characteristics of the BDF: the fraction of the bright, structured gas over the bulk unstructured, faint gas. It is written as the flux ratio of the bright emission to faint emission:

$$\begin{aligned} \mathrm{BDI} &= \log_{10}\left(\frac{\int_{T_2}^{T_3} T \cdot B(T) dT}{\int_{T_0}^{T_1} T \cdot B(T) dT}\right) \\ &= \log_{10}\left(\frac{\sum_{T_2 < T[i] < T_3} T[i]}{\sum_{T_0 < T[i] < T_1} T[i]}\right), \end{aligned} \tag{1}$$

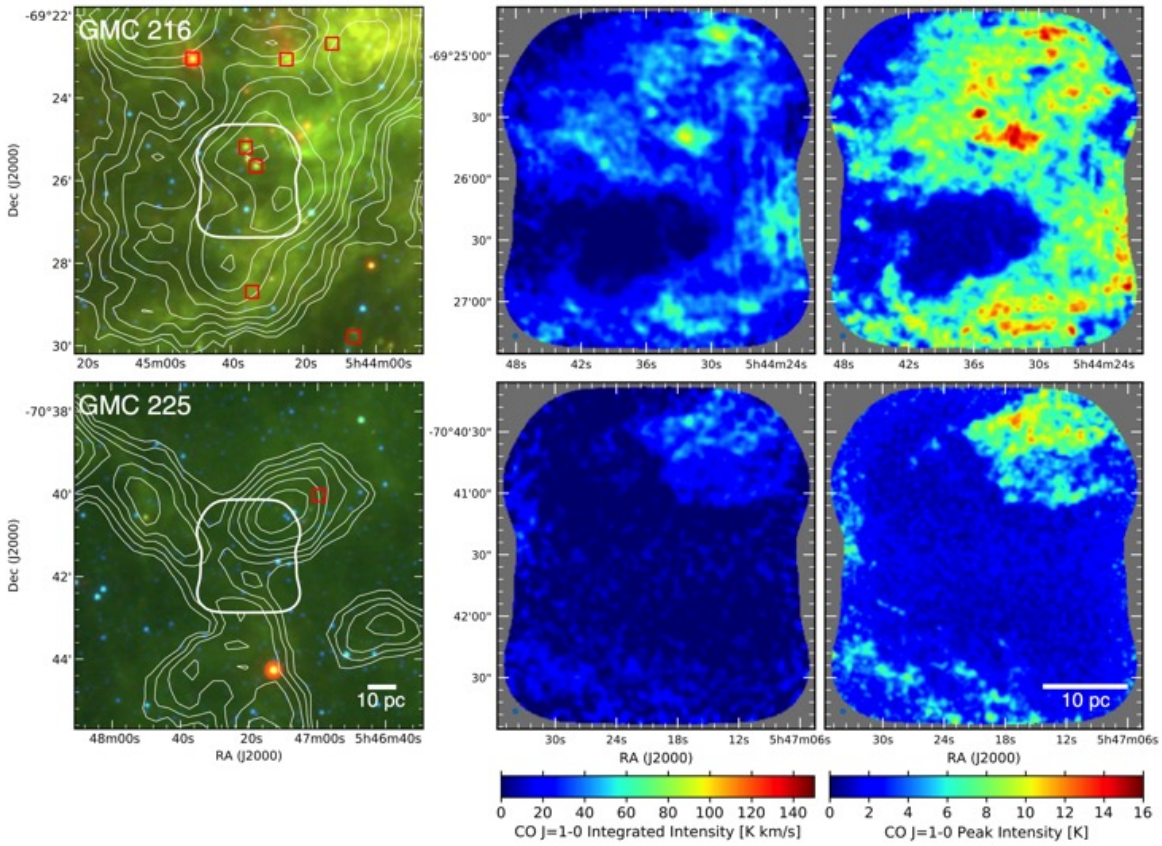

Figure 2. *Continued*

where $B(T)$ denotes the BDF; T_0, T_1, T_2, and T_3 are the brightness thresholds. $T[i]$ is the brightness of the ith pixel in the α–δ–v space. In this paper, we adopt $(T_0, T_1, T_2, T_3) = (3, 5, 10, \infty)$ [K], the same brightness thresholds used for the MW analysis in Sawada et al. (2012a). A high BDI indicates that the gas is structured and has more compact, bright structures.

The BDF/BDI analysis revealed that in the MW disk, structured gas, represented by the high BDI (~ -1 in CO $J = 1$–0 seen at $\simeq 0.7$ pc resolution), is distributed along the spiral arms, while unstructured (low BDI; ~ -3) gas exists in the inter-arm regions. Thus, there is an evolution in gas structure across the spiral arms. Figure 8 (right) shows the BDFs of the molecular gas in the MW around the Galactic longitude of 38° from Sawada et al. (2012a). Assuming the locations of the Sagittarius arm (near and far sides) and inter-arm regions as discussed in Sawada et al. (2012a), the spatial scales are smoothed to match the 0.7 pc resolution of this LMC study. The BDFs of the spiral arms show a tail toward high brightness temperature, while the inter-arm molecular gas does not show the tail. The red and blue shadings are displayed for comparisons with the GMCs in the LMC below. The BDF/BDI analysis has been also applied to external galaxies (Hughes et al. 2013).

We applied the BDF/BDI analysis to the five GMCs. The data are smoothed to a 2 $\mathrm{km\,s^{-1}}$ velocity resolution to achieve better sensitivity. The resultant spatial (0.7 pc) and velocity resolutions and sensitivity (0.37–0.48 K) are comparable to the MW study (Sawada et al. 2012a). Figure 8 (left) shows the BDF of the GMCs. The red and blue shadings are the same as those in the right panel; the red indicates the locus of the BDFs of the spiral arms in the MW, while the blue is for the inter-arm region. GMC 2 is the only GMC without any sign of star formation, and its structure is similar to the quiescent molecular gas in the MW inter-arm regions. Its BDI is very low ($-\infty$; meaning no gas with high brightness > 10 K). The other four GMCs show some signs of star formation, and their BDFs, -1.5 to -0.8, are similar to those of the spiral arms in the MW. The BDIs of the GMCs are shown in the figure legend and Table 2. Although the correlation exists between the high BDI and star formation activity, the cause of the complex structure in molecular clouds is debatable as to whether they are a precursor of star formation or developed by stellar feedback. We, however, note that in the MW high BDI regions do not necessarily coincide with H II regions, and hence indicating the former (Sawada et al. 2012b, see the next subsection).

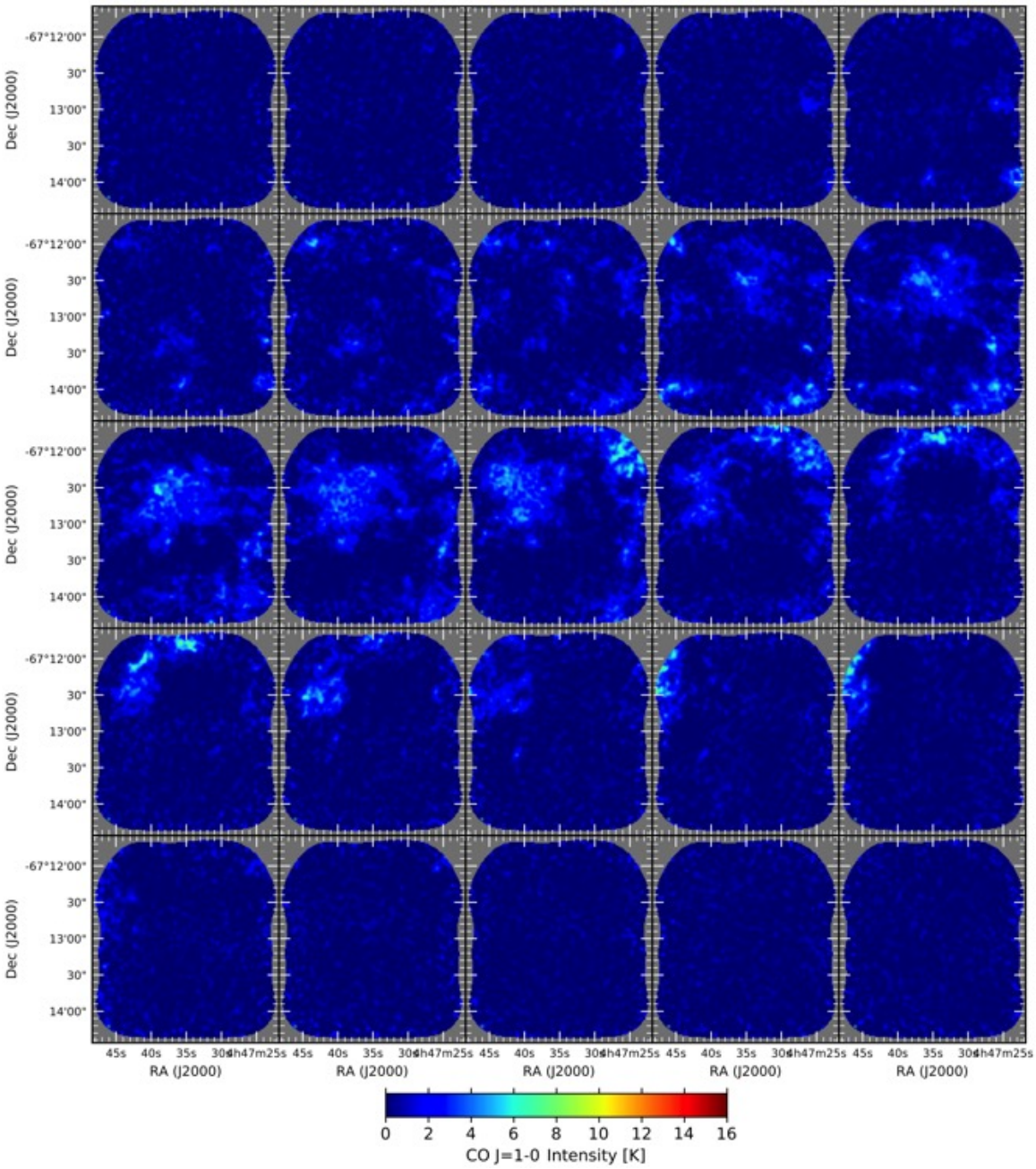

Figure 3. Velocity channel maps of GMC 2 at $v_{\rm LSR}$ = 246, 247, ..., 270 km s^{-1}.

6.2. *Synthesis with Work in the Literature*

Using the BDF/BDI, Sawada et al. (2012b) demonstrated that in the MW, structured gas, represented by a high BDI, is distributed along the spiral arms, while unstructured (low BDI) gas exists in the inter-arm regions (see Figure 8 right). The overall distribution of the high BDI gas is similar to that of the H II regions. They also found some moderately high BDI regions, which are massive molecular concentrations and located in the spiral arms, but without H II regions. These regions may be in the phase between quiescent and active star-forming GMCs. Compact, and presumably dense, structures have already developed in molecular gas, but in which star formation has not yet started. They may be pre-star-forming complexes.

Similar structural differences are present among local star-forming and quiescent molecular clouds. Kainulainen et al. (2009) analyzed the probability distribution function (PDF) of column density derived from the near-infrared dust extinction. They found that the quiescent clouds show a log-normal shape of the PDF as predicted for a turbulent

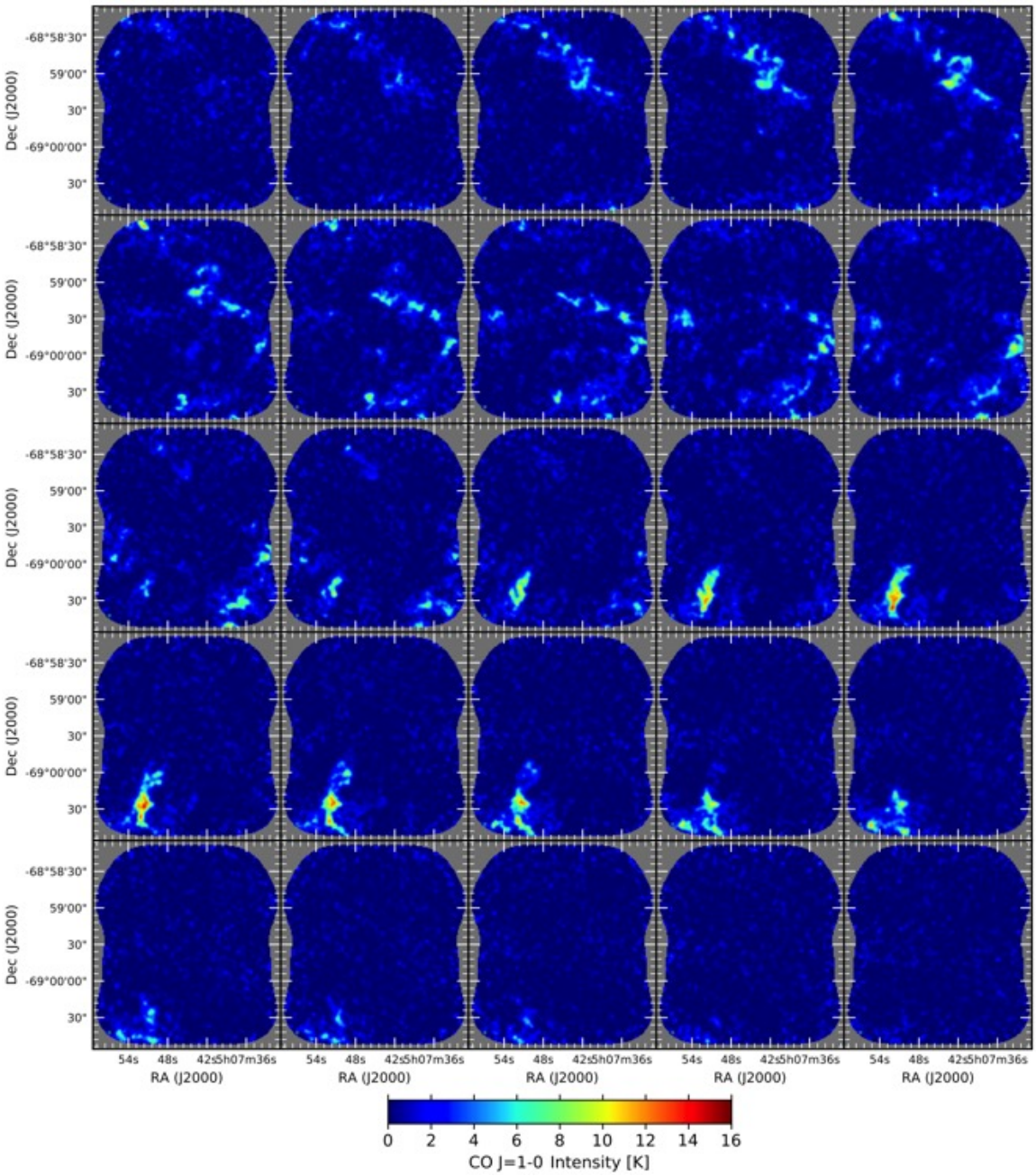

Figure 4. Velocity channel maps of GMC 55 at $v_{\rm LSR}$ = 246, 247, ..., 270 km s^{-1}.

medium, while the star-forming clouds show excess "wings" at higher column densities, presumably due to the self-gravity of dense regions (Klessen 2000; Federrath et al. 2008). The PDF and BDF appear very similar if the CO brightness is converted to column density using the CO-to-H_2 conversion factor. In fact, the PDFs of star-forming and quiescent clouds are *quantitatively* consistent with the BDFs of arm and inter-arm molecular gas, respectively (Sawada et al. 2012a,b). A caveat is that it is not guaranteed that the conversion factor is applicable on a pixel-by-pixel basis. Other optically thin lines, e.g., ^{13}CO or C^{18}O, may trace dense gas better than ^{12}CO, but may miss extended, diffuse gas components (i.e., the denominator of the BDI). It is also possible that the emission lines may not necessarily trace the column/volume density of the gas, but rather the excitation of the spectral lines. We, however, note that Sawada et al. (2012a) found a consistent result with ^{12}CO and ^{13}CO in the BDF analysis in the MW.

Most ALMA studies have been focused on GMCs with active star formation (Figure 1). A quantitative analysis of their data is beyond the scope of this paper, but qualitatively we find a similar trend: structured gas in star-forming clouds and less structured in quiescent clouds. Indebetouw et al. (2013) observed the northern part of 30 Doradus, the

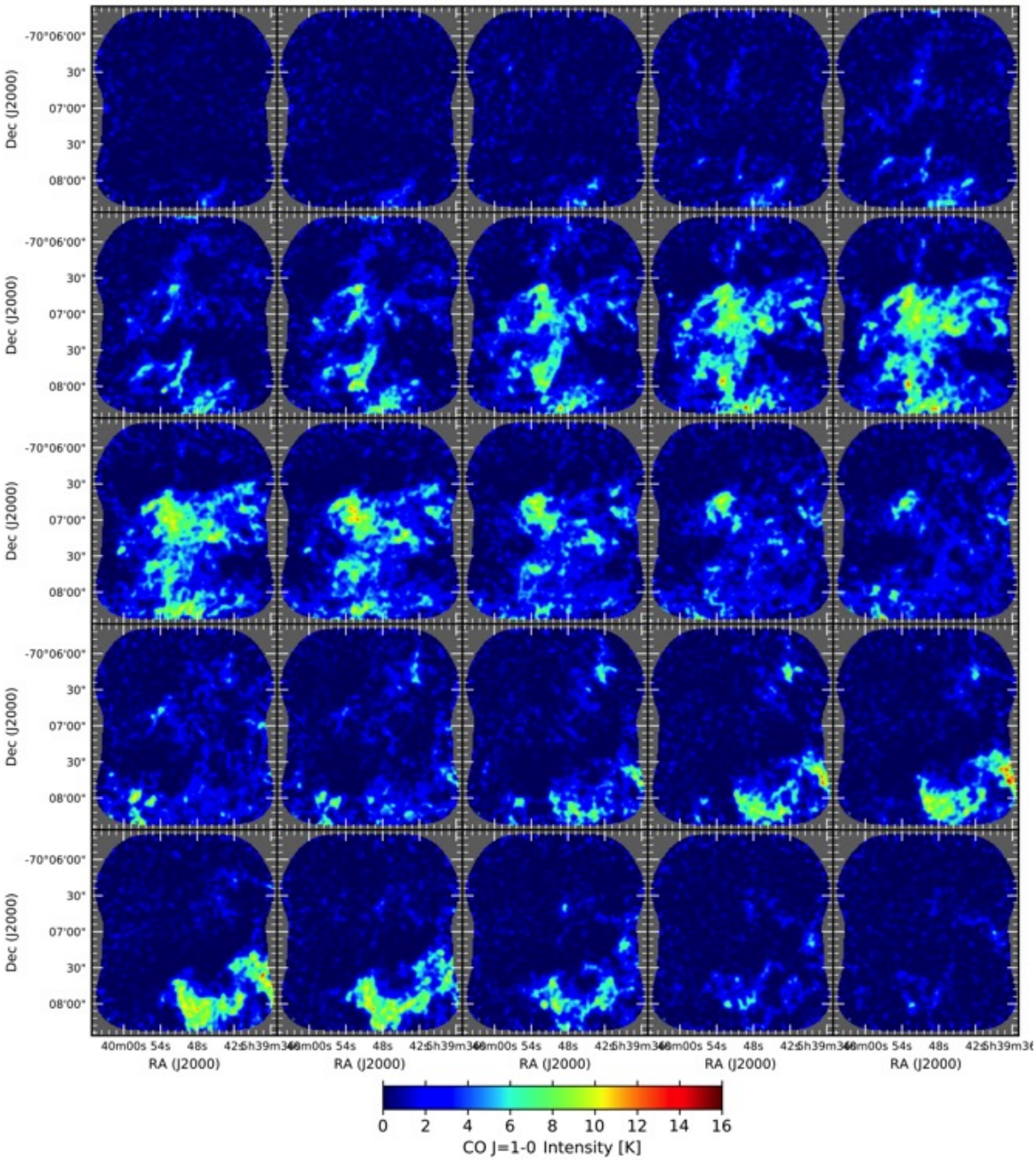

Figure 5. Velocity channel maps of GMC 197 at $v_{\rm LSR}$ = 221, 222, ..., 245 km s^{-1}.

most active star-forming region in the Local Group. In this region, a large fraction of the molecular gas – about 50% – has a brightness temperature above 10 K (see their Figure 4). This cloud has already developed dense structures. In our five GMCs, only the densest clumps have such high brightness temperatures. N159 is another active star-forming region near 30 Doradus that has also been observed with ALMA (Fukui et al. 2015; Saigo et al. 2017; Nayak et al. 2018). The presence of dense clumps and filaments led the authors to speculate on collisions of clouds or filaments as a possible cause of the structures. N55 is an H II region in the largest SGS in the LMC. A cloud near N55 is also very clumpy (Naslim et al. 2018). The same is true in the star-forming cloud N83C in the SMC (Muraoka et al. 2017).

Wong et al. (2017) presented the first ALMA study to contrast star-forming and quiescent molecular clouds in the LMC. They observed a quiescent cloud, designated as the Planck Galactic Cold Clump (PGCC) G282.98−32.40 (Planck Collaboration 2016, Wong et al. called this the "Planck cold cloud" or PCC). It does not show any signs of active massive star formation, and the estimated dust temperature is low ($T_{\rm d}$ ∼15 K). The CO brightness distribution shows a much lower contrast than that in the 30 Doradus cloud and is relatively uniform with only one hotspot. The

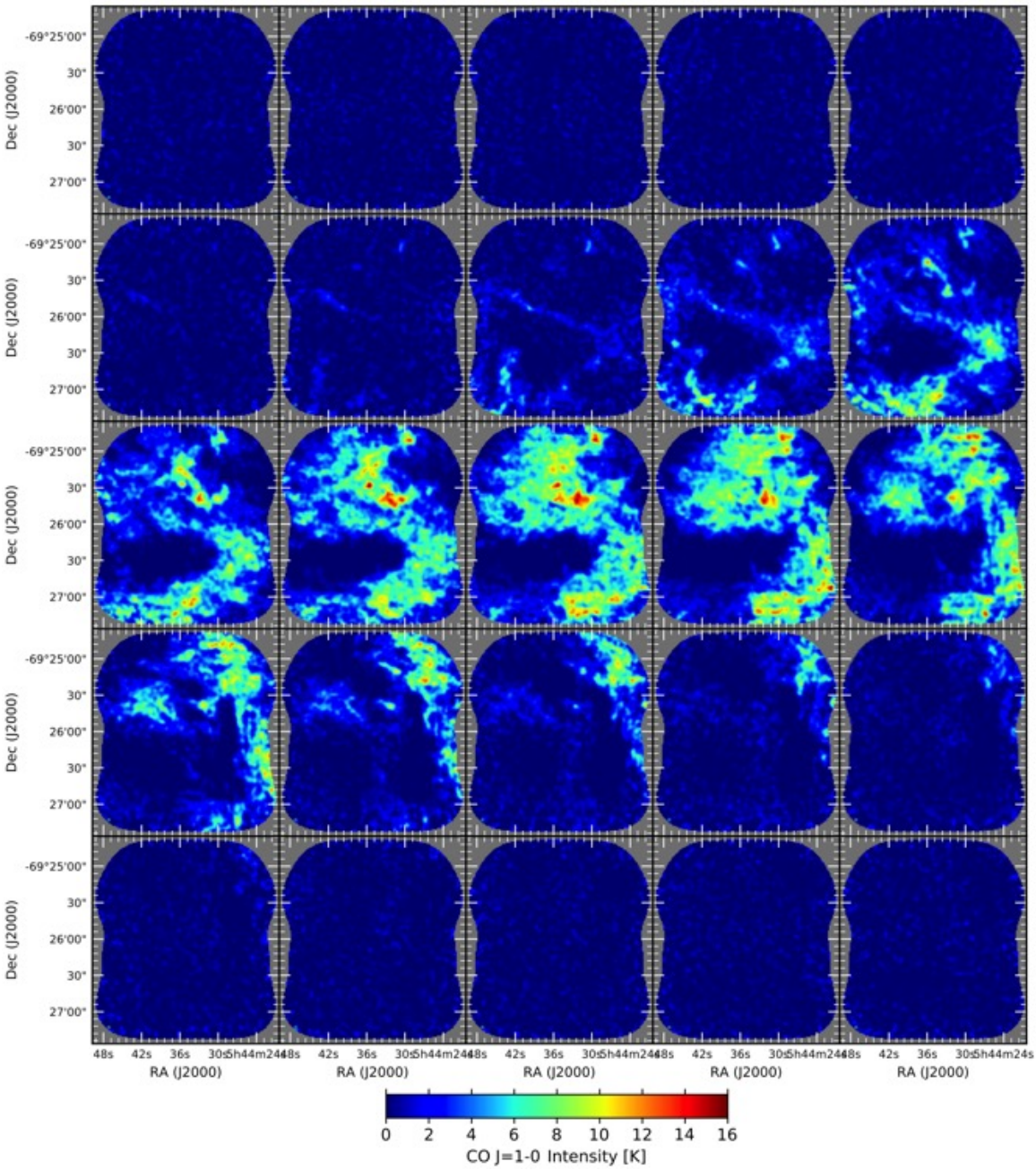

Figure 6. Velocity channel maps of GMC 216 at $v_{\rm LSR}$ = 216, 217, ..., 240 km s^{-1}.

quiescent cloud is less structured.

By synthesizing our five GMCs, one quiescent and four star-forming, with those in the literature, a simple view of a GMC evolutionary sequence is tempting: clouds start from a relatively structureless state, develop complex internal structures, and, as a result, form stars.

6.3. *Caveats*

Of course, this evolutionary sequence in star formation activity may be too simplistic, as other factors, such as environmental triggers, might be at a play. For example, interactions with SGSs may be another important factor (Meaburn 1980; Kim et al. 1999; Yamaguchi et al. 2001; Book et al. 2009; Dawson et al. 2013; Fujii et al. 2014). In fact, GMCs 55, 197, and 216 show relatively high BDIs and are located at the edges of SGS complexes identified by Dawson et al. (2013). The question here is what is the direct cause of the gas with high brightness temperature (perhaps, dense gas). If compression by an SGS directly changes the cloud structure (hence, BDF or PDF) without

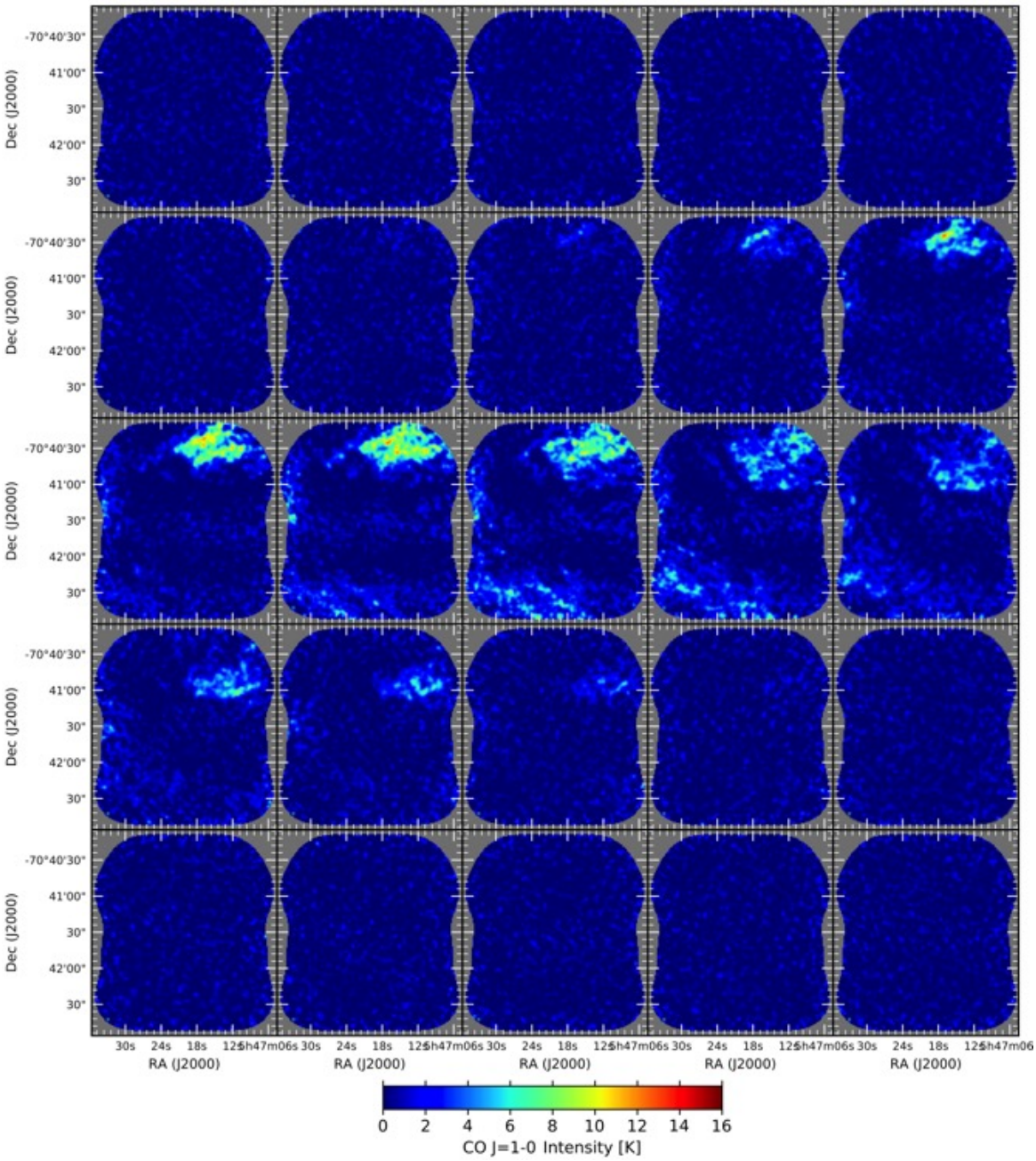

Figure 7. Velocity channel maps of GMC 225 at $v_{\rm LSR}$ = 206, 207, ..., 230 km s^{-1}.

invoking gas self-gravity, we may need to consider its effects separately from the internal physics. The other possible factor is surrounding GMCs. Figure 2 (left) shows that some of the GMCs in Fukui et al. (2008) are GMC complexes rather than single GMCs. These are some of the reasons why even the relatively large ALMA mosaics ($\approx$ 40 pc) are not enough to cover the entire emission. If the surrounding GMCs trigger compression, e.g., by tides or collisions, the environment would be another factor to consider. Studies into multiple factors clearly require a much larger sample of GMCs in the LMC. Such statistics should be possible with ALMA as it is approaching its operational maturity.

This paper makes use of the following ALMA data: ADS/JAO.ALMA#2012.1.00641.S. ALMA is a partnership of ESO (representing its member states), NSF (USA) and NINS (Japan), together with NRC (Canada), MOST and ASIAA (Taiwan), and KASI (Republic of Korea), in cooperation with the Republic of Chile. The Joint ALMA Observatory is operated by ESO, AUI/NRAO and NAOJ. This research made use of Astropy, a community-developed core Python package for Astronomy (Astropy Collaboration et al. 2013). This research made use of Montage. It

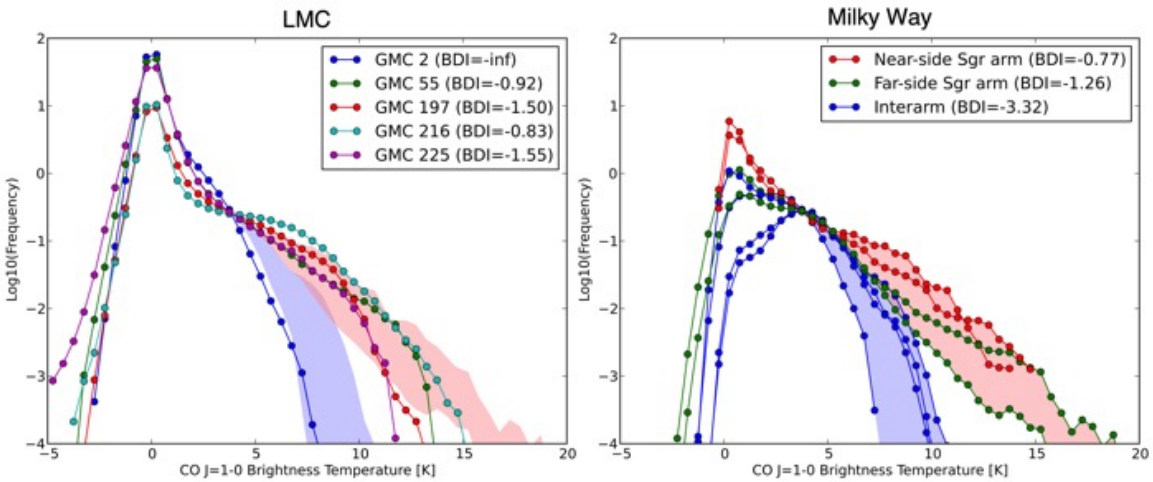

Figure 8. Left: the brightness distribution functions (BDFs) of GMCs 2, 55, 197, 216, and 225. The frequency is normalized by the number of the pixels with 3–5 K intensity. The red and blue shaded regions are the BDFs of the spiral arm and inter-arm regions of the Milky Way (see the right panel). Right: the BDFs of the gas in the Milky Way. The data (Sawada et al. 2012a) are smoothed to match the spatial resolution of the ALMA data (0.73 pc). Four 5 $\mathrm{km\,s^{-1}}$ velocity bins were taken for the arm (v_{LSR} = 40–45, 45–50 $\mathrm{km\,s^{-1}}$ for the nearside Sgr arm; 55–60, 60–65 $\mathrm{km\,s^{-1}}$ for the farside Sgr arm) and inter-arm regions (75–80, 80–85, 85–90, and 90–95 $\mathrm{km\,s^{-1}}$), respectively.

is funded by the National Science Foundation under grant number ACI-1440620, and was previously funded by the National Aeronautics and Space Administration's Earth Science Technology Office, Computation Technologies Project, under Cooperative Agreement Number NCC5-626 between NASA and the California Institute of Technology. J.K. acknowledge the support from the NSF under grant AST-1211680. We thank J. Barrett for improving the manuscript.

Facilities: ALMA, Mopra, *Spitzer*

Software: CASA (McMullin et al. 2007), Miriad (Sault et al. 1995), Astropy (Astropy Collaboration et al. 2013)

REFERENCES

Astropy Collaborations, Robitaille, T. P., Tollerud, E. J., et al. 2013, A&A, 558, A33
Book, L. G., Chu, Y.-H., Gruendl, R. A., & Fukui, Y. 2009, AJ, 137, 3599
Claude, S., Jiang, F., Niranjanan, P., et al. 2008, Proc. SPIE, 7020, 70201B
Dawson, J. R., McClure-Griffiths, N. M., Wong, T., et al. 2013, ApJ, 763, 56
Escoffier, R. P., Comoretto, G., Webber, J. C., et al. 2007, A&A, 462, 801
Federrath, C., Klessen, R. S., & Schmidt, W. 2008, ApJL, 688, L79
Fujii, K., Minamidani, T., Mizuno, N., et al. 2014, ApJ, 796, 123
Fukui, Y., Harada, R., Tokuda, K., et al. 2015, ApJL, 807, L4
Fukui, Y., Kawamura, A., Minamidani, T., et al. 2008, ApJS, 178, 56
Gordon, K. D., Roman-Duval, J., Bot, C., et al. 2014, ApJ, 797, 85
Grenier, I. A., Casandjian, J.-M., & Terrier, R. 2005, Science, 307, 1292
Henize, K. G. 1956, ApJS, 2, 315
Hills, R. E., Kurz, R., J., & Peck, A. B. 2010, Proc. SPIE, 7733, 773317
Hughes, A., Meidt, S. E., Schinnerer, E. et al. 2013, ApJ, 779, 44
Iguchi, S., Morita, K.-I., Sugimoto, M., et al. 2009, PASJ, 61, 1
Indebetouw, R., Brogan, C., Chen, C.-H. R., et al. 2013, ApJ, 774, 73
Jorsater, S. & van Moorsel, G. A. 1995, AJ, 110, 2037
Kainulainen, J., Beuther, H., Henning, T., & Plume, R. 2009, A&A, 508, 35
Kamazaki, T., Okumura, S. K., Chikada, Y., et al. 2012, PASJ, 64, 29
Kawamura, A., Mizuno, Y., Minamidani, T., et al. 2009, ApJS, 184, 1
Kim, S., Dopita, M. A., Staveley-Smith, L., & Bessell, M. S. 1999, AJ, 118, 2797
Kim, S., Staveley-Smith, L., Dopita, M. A. et al. 2003, ApJS, 148, 473
Klessen, R. S. 2000, ApJ, 535, 869
Koda, J., Scoville, N., Sawada, T., et al. 2009, ApJL, 700, L132
Koda, J., Sawada, T., Wright, M. C. H., et al. 2011, ApJS, 193, 19
Lada, C. J. & Lada, E. A. 2003, ARA&A, 41, 57
McMullin, J. P., Waters, B., Schiebel, D., Young, W., & Golap, K. 2007, in ASP Conf. Ser. 376, Astronomical Data Analysis Software and Systems XVI, ed. R. A. Shaw, F. Hill, & D. J. Bell (San Francisco, CA: ASP), 127
Meaburn, J. 1980, MNRAS, 192, 365
Meixner, M., Gordon, K. D., Indebetouw, R., et al. 2006, ApJ, 132, 2268
Muraoka, K., Homma, A., Onishi, T., et al. 2017, ApJ, 844, 98
Naslim, N., Tokuda, K., Onishi, T., et al. 2018, ApJ, 853, 175
Nayak, O., Meixner, M., Fukui, Y., et al. 2018, ApJ, 854, 154

Pietrzyński, G., Graczyk, D., Gieren, W., et al. 2013, Nature, 495, 76
Planck Collaboration, Ade, P. A. R., Aghanim, N., et al. 2011, A&A, 536, A19
Planck Collaboration, Ade, P. A. R., Aghanim, N., et al. 2016, A&A, 594, A28
Saigo, K., Onishi, T., Nayak, O., et al. 2017, ApJ, 835, 108
Sault, R. J., Teuben, P. J., & Wright, M. C. H. 1995, in ASP Conf. Ser. 77, Astronomical Data Analysis Software and Systems IV, ed. R. A. Shaw, H. E. Payne, & J. J. E. Hayes (San Francisco, CA: ASP), 433
Sawada, T., Hasegawa, T., & Koda, J. 2012a, ApJL, 759, L26
Sawada, T., Hasegawa, T., Sugimoto, M., Koda, J. & Handa, T. 2012b, ApJ, 752, 118
Schinnerer, E., Meidt, S. E., Pety, J., et al. 2013, ApJ, 779, 42
Seale, J. P., Meixner, M., Sewiło, M., et al. 2014, AJ, 148, 124
Staveley-Smith, L., Kim, S., Calabretta, M. R., Haynes, R. F., & Kesteven, M. J. 2003, MNRAS, 339, 87
van der Marel, R. P. & Cioni, M.-R. L. 2001, AJ, 122, 1807
Wong, T., Hughes, A., Ott, J., et al. 2011, ApJS, 197, 16
Wong, T., Hughes, A., Tokuda, K., et al. 2017, ApJ, 850, 139
Yamaguchi, R., Mizuno, N., Onishi, T., Mizuno, A., & Fukui, Y. 2001, PASJ, 53, 959